Evidence of in-depth incorporation of carbon nanotubes in alumina layers grown by plasma electrolytic oxidation

C. da Silva Tousch, J. Martin, G. Marcos, T. Czerwiec, G. Henrion

To cite this version:

C. da Silva Tousch, J. Martin, G. Marcos, T. Czerwiec, G. Henrion. Evidence of in-depth incorporation of carbon nanotubes in alumina layers grown by plasma electrolytic oxidation. Surface and Coatings Technology, 2022, 440, pp.128489. 10.1016/j.surfcoat.2022.128489 . hal-03866766v1

HAL Id: hal-03866766
https://hal.science/hal-03866766v1

Submitted on 26 Jan 2023 (v1), last revised 22 Nov 2022 (v2)

Evidence of in-depth incorporation of carbon nanotubes in alumina layers grown by plasma electrolytic oxidation

C. Da Silva Tousch[1], J. Martin[1,2*], G. Marcos[1,2], T. Czerwiec[1,2], G. Henrion[1,2]

[1] Université de Lorraine, CNRS, IJL, F-54000 Nancy, France

[2] Université de Lorraine, Laboratoire d'Excellence Design of Alloy Metals for low-mAss Structures ('LabEx DAMAS'), F-57045 Metz, France

*Corresponding author: +33 (0)3.72.74.24.97, julien.martin@univ-lorraine.fr

Abstract

Incorporation of carbon nanotubes (CNTs) into ceramic layers during plasma electrolytic oxidation (PEO) is promising for direct synthesis of composite protective coating on lightweight metallic alloys. In the present study, complementary characterization techniques were used in order to definitively assess the presence of CNTs through the thickness of a PEO alumina coating formed in a silicate-based electrolyte containing dispersed multi-walled carbon nanotubes (MWCNTs). Cross-checked results helped in evidencing that MWCNTs are partially incorporated in the thickness of the PEO alumina coating, and more precisely through the porous outer sublayer. They were mainly found in the form of scaffolds that line the interior walls of pores. To a lesser extent, some individual MWCNTs were found interlocked in the fine grain structure of alumina. The analysis of the specific Raman bands of MWCNTs also highlighted that incorporation is associated with an alteration of the structural integrity of the MWCNTS. It was also established that the increase in the amount of dispersed MWCNTs results in a thicker but more porous CNTs-enriched PEO coating. Based on the collected results, some precisions regarding the incorporation mechanisms were proposed.

Keywords: Aluminum; Carbon nanotubes (CNTs); Plasma Electrolytic Oxidation (PEO); Micro-Arc Oxidation (MAO); Alumina coating; Incorporation mechanism

1. Introduction

Plasma electrolytic oxidation (PEO), sometimes referred to as micro-arc oxidation (MAO), is a plasma-assisted electrochemical surface treatment particularly suited to convert aluminum into a protective alumina layer. PEO differs significantly from acid anodizing processes since it is conducted under higher voltages/currents and oxidation results from the apparition of micro-discharges issued from the electric breakdown of the growing oxide layer. The resulting coating provides increased hardness, wear protection and corrosion resistance [1]. Although PEO coatings are usually porous [2], this intrinsic feature can be seen as providing new opportunities for incorporating various kinds of elements or particles in the course of the process or post-process [3]. Indeed, it is now well established that dissolved species in the electrolyte such as Si, Na and K penetrate throughout the coating [4]. Several process parameters, especially the electrolyte chemistry and the applied electrical parameters [5], can be tuned in order to promote the formation of porous PEO coatings with high specific surface area, thus amplifying the adsorption mechanism of these dissolved species.

More interestingly, the porous nature of the formed oxide layer stemmed an interest in incorporating solid particles to enhance its protective properties or even introduce new emerging properties. To achieve this goal, micro- or nano-particles are dispersed in the electrolyte before carrying out the PEO process with the intent of continually incorporating them during the growth of the coating. It results in the formation of an oxide-based composite coating whose microstructure is directly influenced by the composition, the size and the concentration of the dispersed particles. For example, several studies have investigated PEO treatments in electrolytes containing metallic or metal-oxide particles [6, 7]. From those studies, three main conclusions can be drawn.

(i) The incorporation of solid particles can be distinguished as either reactive or inert. In the case of reactive incorporation, the size, the shape, the chemical composition and the microstructure of the incorporated particles are severely altered. This is more pronounced for nano-particles [8, 9] and for particles having a low melting temperature [10–12]. The generally accepted assumption is that the solid particles melt when locally exposed to the high temperature induced by the micro-discharges, and react chemically with the elements from the electrolyte and the substrate. Conversely, in the case of inert incorporation, the particles found in the pores of the coating remain majorly unaltered. This is mainly observed for particles exhibiting high melting temperatures [13–15] and high mass [6].

(ii) The mechanisms of incorporation generally agreed upon are electrophoresis and mechanical insertion. Electromigration particularly concerns the colloidal suspensions, inside which particles are characterized by their zeta potential. When subjected to an electric field, particles of the colloidal suspension migrate towards either electrode depending on the sign of their zeta potential [16]. In the context of the PEO process, particles exhibiting a negative zeta potential will be preferentially drawn towards the anode where the oxidation reaction occurs, and therefore promote their incorporation into the growing PEO oxide coating. On the other hand, the specific mechanism of the mechanical insertion results from the dynamics of apparition and extinction of micro-discharges on the surface of the substrate that induces repetitive expansion and cavitation of the plasma bubbles. This is accompanied with variations of the fluid pressure that are suspected to drag and entrap particles into the pores of the coating [17]. It implies that the efficiency of this mechanical insertion is directly dependent on the size of the dispersed particles; their dimensions must thus be smaller than that of the pores. Given that pores are typically of the micrometer scale, particles in the micron size range cannot effectively penetrate into pores and have a tendency to deposit on the extreme surface only, obstructing the outer pores [3, 9].

(iii) The presence of dispersed particles into the electrolyte as well as those already incorporated into the oxide layer alters the electrical response of the PEO process. Indeed, depending on their nature, it has been shown that particles modify the dielectric breakdown conditions of the growing coating, the characteristics of the micro-discharges and finally the morphology of the produced oxide coating [7]. Nevertheless, no general conclusions can be drawn due to the wide range of different PEO processing conditions reported in the literature. On the other hand, the applied electrical conditions themselves have an impact on the particles. PEO treatment conducted using high power promotes the reactive incorporation of nano-particles with low melting temperature since more energy is provided to heat up and melt them. Inversely, when diminishing the applied power to the PEO electrolyser system, the inert incorporation is favored given that not enough energy is available to melt the particles [18].

The present study focuses on carbon-based nano-particles and more specifically carbon nanotubes (CNTs). Due to their exceptional mechanical and electrical properties [19], CNTs have numerous applications as structural reinforcements in various composite structures [20, 21]. Most notably, polymer-based composites reinforced with CNTs have had a noteworthy development resulting in materials with tunable properties [22]. Metallic matrix composites as well as reinforced ceramics have also been reported, although to a lesser extent [23, 24]. Although the tribological properties and corrosion behavior of the formed oxide were evaluated, little evidence was provided to finely characterize the presence of CNTs throughout the oxide layer [25–30]. As a matter of fact, few studies involving the PEO treatment of aluminum in an electrolyte containing CNTs were published. Yürektürk et al. reported a decrease in coating thickness, a denser surface and a decrease in surface pores leading to higher hardness and better wear resistance for coatings processed with CNTs [31]. A lower porosity and a denser layer allowing better corrosion resistance were reported by Lee et al. [32]. On the other hand, Sabouri et al. observed a detrimental effect of MWCNT incorporation on the compactness of the coating, leading to a decrease in the protective properties of the coating [33]. Lee et al. also observed that an increase in current density led to an increase in incorporated MWCNT and a decrease in surface micro-pores [34]. In some cases, the surface morphology of the PEO coatings formed in the presence of MWCNTs did not display the typical pancake-like structures of PEO coatings [35]. All these works also mention a decrease in breakdown voltage in the presence of CNTs attributed to the high electrochemical capacity of the CNTs. Finally, the main driving force for CNT incorporation suggested in all studies is electrophoresis, based on Zeta potential measurements of the CNTs dispersions indicating a negative surface charge, which would thus imply that the CNTs are drawn towards the anode during the PEO process. Also, those studies mainly reported the presence of CNTs from the top surface examination of the samples without much evidence of an in-depth incorporation of the CNTs. If up to now, no strong evidence of an in-depth incorporation was demonstrated, it might be explained by the fact that the porous nature of the PEO alumina, combined with limitations regarding reliably detecting carbon, pose major obstacles to finely characterize this incorporation. In the present work, complementary characterization techniques, including high resolution scanning electron microscopy (SEM), micro-Raman spectroscopy, glow discharge optical emission spectroscopy (GDOES) and transmission electron microscopy (TEM) equipped with an energy dispersive X-ray (EDX) facility, were used to finely detect the presence of CNTs throughout the PEO oxide layer to get new insights into the mechanism of their incorporation.

2. Materials and methods

PEO was performed on pure aluminum alloy (series 1050) whose elemental composition is given in Table I. Prior to processing, samples were cut into a rectangular cuboid of dimensions 5 × 15 × 50 mm^3 corresponding to a processed surface of about 21.5 cm^2. Samples were then polished to 1200 grit and thoroughly rinsed with acetone then ethanol, and dried before any experiment.

A dry powder of multiwalled carbon nanotubes (MWCNTs) was provided by Arkema (Graphistrength C100). MWCNTs were produced using a catalytic chemical vapor deposition (CCVD) route. As described in Table II, their initial characteristics were estimated from SEM, thermogravimetric analysis (TGA) and TEM measurements. The powder consists of large spherical aggregates of about 200 to 1000 µm in diameter in which MWCNTs are intertwined. The average external diameter of the MWCNTs is between 12 nm and 20 nm and their length extends from 0.1 to 10 µm. Their purity was assessed by TGA under air flow from 20 °C up to 1100 °C with a temperature ramp of 3 °C/min. From TGA measurements, the total carbon content was estimated at 93 %wt. The remaining weight only corresponds to iron catalysis particles that are required for the CCVD synthesis route.

Regarding the electrolyte, a standard base solution containing 1 g.L^{-1} KOH and 1.65 g.L^{-1} Na_2SiO_3 diluted in deionized water was prepared. Its electrical conductivity and pH were 8.5 mS.cm^{-1} and 13, respectively. From this stock solution, and as described in Table III, various solutions were then prepared by dispersing MWCNTs in concentrations of 0, 1, 2 and 3 g.L^{-1}. In the following, samples processed within these solutions are referred to as S0, S1, S2 and S3, respectively. A special care was required to properly disperse and stabilize the suspension of MWCNTs in the electrolyte. This was achieved by submitting the suspension to probe sonication. The propagation of energetic acoustic shockwaves allows breaking aggregates into detangled CNTs. However, given their hydrophobic nature, non-functionalized carbon nanoparticles have a strong tendency to reaggregate when dispersed in water [36]. In order to maintain a stable suspension, an amphiphilic compound was added to the solutions. As noted in Table III, sodium dodecyl sulfate (SDS) was used and dissolved in various concentrations to maintain a constant ratio between the concentration of MWCNT and that of SDS. The suspension was evaluated by Zeta potential measurement. A mean value of -46.3mV with standard deviation or 1.9 mV was obtained. As the absolute value of Zeta potential is greater than 30 mV, the suspension is considered physically stable [37]. Finally, to avoid sedimentation of the dispersed MWCNTs during the PEO process, PEO treatments were carried out in a 2 L beaker that was itself positioned in an ultrasonic tank.

PEO treatments were performed in a home-made experimental set-up. The power unit consists of a current generator that supplies the electrode with a bipolar current waveform. In the present study, a symmetrical current waveform was applied to the electrodes resulting in an anodic to cathodic charge quantity ratio equal to 1 [38]. The anodic amplitude of the current was set at 10 A in order to provide an anodic current density of 50 $A.dm^{-2}$ on the treated sample. The current pulse frequency was maintained at 100 Hz and the positive and negative pulses were identical quasi-square pulses. The detailed parameters of the applied electrical parameters are summarized in Fig. 1. The counter electrodes consisted of titanium plates with 100 × 50 mm^2 dimensions. The temperature of the electrolyte was maintained at 65 °C by a copper coil surrounding the processed sample in which water flowed at 17 °C. All samples were processed for 20 minutes. After PEO treatment, samples were immediately removed from the electrolyte, thoroughly rinsed with distilled water and finally dried under a warm air stream.

Morphology of the produced PEO coatings was observed from top-surface and cross-section views using a field emission gun scanning electron microscope (ZEISS GeminiSEM 500) working in the conventional secondary electron mode (SE) as well as in the InLens mode. Contrary to the standard SE detector positioned at an angle relative to the electron source to obtain topographical information of the sample surface, the InLens detector is located in line with the field emission gun, perpendicular to the surface of the sample [39]. This allows high resolution observations at high magnification within the pores both in top-views and cross-sections. Moreover, it was observed that with InLens imaging mode, the interaction between the electrons and the MWCNTs induces a very intense signal collected by the InLens detector thus making it easy to detect them even at low magnification. Prior to cross-section SEM observations, samples were cut and gradually polished to achieve a mirror-like surface aspect. To avoid any measurement artifacts induced by a polymer mounting resin in the detection of the carbon element, cut samples were not mounted in resin. Unless mentioned otherwise, the average thickness of coatings was evaluated by considering ten measurements over the cross-section. Roughness measurements were performed at the center of each processed sample. The average mean roughness parameter of the coating (Ra) was assessed using a Bruker DektakXT stylus profilometer with lateral and depth resolutions of 0.2 µm and 1 nm, respectively.

Raman spectroscopy was performed on a confocal micro-Raman spectrometer (HR800 Horiba) using a 1800 grooves/mm grating and a laser wavelength of 532 nm. Within the considered wavenumber range from 1000 to 3500 cm^{-1}, this excitation wavelength induces a photoluminescent response from the PEO alumina that does not directly interfere with the Raman bands from the MWCNTs. MWCNTs being concentric cylindrical graphene sheets, they present: (i) a strong peak around 1580 cm^{-1} (G band) from the high frequency first-order mode (E_{2g}), (ii) another strong peak around 1350 cm^{-1} (D band) resulting from a hybridized vibrational mode associated with edges and disorder in the structure, and (iii) a weaker band around 1620 cm^{-1} (D' band). The second order part of the Raman spectra of MWCNTs includes the scattering bands around 2450 cm^{-1} (D+D"), 2700 cm^{-1} (2D or G'), 2945 cm^{-1} (D+D') and 3175 cm^{-1}(2G) [40]. The intensity of the D band is considered as structural defect dependent. According to the double resonance theory, the crystal defects and the crystal edges scatter the excited electrons, which explain that the more defects are present in the MWCNTs, the more intense the D band gets [41]. The intensity ratio of the D band ~1350 cm^{-1} and the G band ~1590 cm^{-1} thus allows one to comparatively evaluate the structural integrity of the MWCNTs [42]. Two other bands on the typical spectrum of MWCNTs are the D" band (also known as D4 band) and the $G_{amorphous}$ band (also known as D3 band), which are respectively located at ~1150 cm^{-1} and ~1500 cm^{-1}. The D" band is a shoulder to the D band that has been attributed to the presence of carbon soot and other amorphous carbon [43]. Regarding the $G_{amorphous}$band, it originates from the presence of disordered carbons [44]. This peak is extrapolated from the mathematical spectral decomposition of the Raman spectrum and a direct impact of its intensity is illustrated on the spectrum in the region between the D and G peaks: the elevation compared to the baseline is partially influenced by the intensity of the $G_{amorphous}$ peak. The main information regarding the band name, position and interpretation of MWCNT Raman peaks are summarized in Table IV.

Glow discharge optical emission spectroscopy (GDOES) was performed on a Horiba Profiler 1000RF. The characterized samples were placed in an enclosing bell in order to ensure stable analysis conditions. It is worth mentioning that the intrinsic roughness and porosity of the PEO oxide layers imply that the signal collected over time is not purely linked to a particular depth of erosion. For this reason, the GDOES element profiles are presented as a function of the sputtering time rather than the erosion depth. Thus, the elemental profile is a qualitative representation of the presence of the different elements through the coating depth.

Regarding TEM observations, structure of the elaborated oxide layers was investigated using a JEOL ARM 200F – cold FEG UHR- transmission electron microscope operating at 200 kV and equipped with a Cs corrector. In scanning mode (STEM), EDX analyses were obtained using a JEOL CENTURIO energy-dispersive X-ray spectrometer. EDX element distribution maps recorded over an area of 512 nm × 512 nm (one measurement point per nm), were produced by using an acquisition time of 1 ms per measurement point and by repeating 20 scans over the same area. The specimen for TEM was extracted from a MWCNTs-containing PEO alumina coating using the micro-cleaving procedure. According to this procedure, the surface of the PEO processed sample was scratched with a diamond knife in order to break off micro-grains from the oxide coating that were then transferred onto a TEM grid for examination. TEM allowed observing the aggregation state and the dimensions of the MWCNTs. Also, HRTEM revealed the integrity of the carbon nanotube walls and extremities. Finally, it is worth noting that for comparison reasons, the as-received MWCNTs were also observed with TEM using a PHILIPS CM 200 FEG microscope. To achieve this, they were dispersed at low concentration in pure ethanol, a drop of which was deposited on a TEM grid and was left to dry until total evaporation of ethanol before observation.

3. Results and discussion

3.1 Degradation of the MWCNTs

The potential degradation of the MWCNTs dispersed in the electrolyte is a concern, especially when successive samples are PEO processed within the same electrolyte bath. Indeed, several factors such as the PEO processing time and parameters may irreversibly affect the electrolyte and dispersed particles, thus making reproducibility and comparison between samples difficult.

Probe sonication has been shown to induce mechanical degradation of the particles [45]. The ultrasonic vibration generates cavitation of bubbles that rapidly expand and implode. It induces variations of the pressure stresses on the MWCNTs aggregates that allow dispersing the intertwined MWCNTs. However, the major drawback of the probe sonication technique is that the high energy transferred to the particles could also lead to their structural degradation by fracture and fragmentation.

TEM examination (Fig. 2) confirms the efficiency of the probe sonication technique regarding disaggregation. Indeed, the intertwined nanotube aggregates are effectively separated without any significant degradation regarding their length or diameter. Raman spectroscopy revealed no major alteration regarding the spectral response of the dispersed MWCNTs after ultrasonic dispersion. However, the PEO treatment may affect the MWCNTs. Indeed, Fig. 3 displays the Raman spectra of the as-received MWCNTs and the MWCNTs collected from the electrolyte after 20 min of PEO treatment and complete drying. The calculated average ID/IG intensity ratio over five measures in each case gives 1.19 for the as-received MWCNTs and 1.21 for the MWCNTs collected from the electrolyte after 20 min of PEO treatment. The minor variation can be attributed to statistical variance. However, it can be mentioned that the D’ band that is a shoulder of the G band, is noticeably more detectable on the spectra collected after sonication dispersion and after PEO treatment. This observation indicates a slightly higher defect density within the particles after those steps [46]. Additionally, after the PEO treatment, the D” and the $G_{amorphous}$ bands increase in intensity indicating an increase in the proportion of soot and amorphous carbons. It suggests that a significant amount of the MWCNTs initially introduced in the electrolyte became amorphous during the PEO process [47]. One explanation consists in considering the local temperature nearby micro-discharges that was estimated up to 3200 K, in the range of the sublimation temperature of MWCNTs. After extinction of the micro-discharge, the melted MWCNTs particles are rapidly quenched by the cooled electrolyte and solidified into an amorphous structure [48].

These observations indicate that the dispersed MWCNTs are affected by the different processing steps. It is thus questionable whether the electrolyte with dispersed MWCNTs could be re-used multiple times. Consequently, a new electrolyte was prepared from the stock solution for each experiment.

3.2 Top-surface characterization

Fig. 4 shows the visual aspect of the samples processed with various concentrations of MWCNTs dispersed in the electrolyte. Sample S0 treated without MWCNTs appears white. The increase in MWCNTs concentration results in a significantly darker aspect suggesting a higher proportion of carbon on the processed surface. Sample S1 treated with 1 $g.L^{-1}$ has a gray aspect with a few localized dark spots while samples S2 and S3 processed with higher concentrations of MWCNTs present increasingly larger dark regions randomly distributed over the entire surface. For S3, dark regions dominate throughout the surface.

In Fig. 5, top-surface SEM micrographs also evidence differences regarding the morphology of the processed surfaces. The surface of sample S0 treated without MWCNTs exhibits an arrangement of “pancake-like” structures uniformly distributed over the surface, as usually encountered for PEO alumina coatings elaborated in silicate-based electrolyte [49]. In contrast, the surface of samples treated with MWCNTs reveals an alternance of smoother and rougher regions next to each other. For these latter, numerous large and deep jagged structures are visible (evidenced in red in Fig. 5 for S2 sample). The presence of MWCNTs in the electrolyte locally induces the formation of a more rugged surface. These preliminary observations were confirmed by roughness measurements carried out on each sample. Average roughness value Ra for samples S0, S1, S2 and S3 is given in Table V. This roughness parameter increases by a factor of 3 between the reference sample S0 treated without MWCNTs and the sample S3 treated with a MWCNTs concentration of 3 $g.L^{-1}$.

Fig. 6 shows SEM micrographs recorded using the InLens mode on the top-surface of the samples S1 and S3. Using the InLens mode, the presence of MWCNTs on the surface can more easily be observed and is indicated by red circles and arrows in Fig. 6. Despite the efforts made to efficiently disperse MWCNTs in the electrolyte, their spatial distribution over the surface of the PEO processed samples is not homogeneous. Indeed, some locations are fully lined with MWCNTs scaffolds while the surface coverage in other regions is more scarce. In that regard, Fig. 6 A, B illustrate differences in the MWCNTs distribution between the samples S1 and S3. The amount of MWCNTs found on the surface clearly increases as the concentration of dispersed MWCNTs in the electrolyte increases. For sample S1, large regions are depleted of MWCNTs while they cover more homogeneously the surface of the sample S3. Regions with concentrated MWCNTs scaffolds (circled in red in Fig. 6 A) corresponds to the darker regions on the processed samples, as observed in Fig. 4. At higher magnification, MWCNTs are also observed inside pores and cracks, suggesting an impregnation of MWCNTs deeper in the open porosity of the PEO coating.

Raman spectra recorded on the surface of the processed samples (Fig. 7) confirm that the nano-particles observed from top-surface of the samples S1, S2 and S3 definitively consists of MWCNTs since their distinctive Raman scattering bands are clearly identified. The two most distinguishable peaks D and G, as well as the 2D peak are detected, especially in the darker regions where particles are more concentrated. For the sample S0, treated without MWCNTs, the distinctive Raman bands of the MWCNTS are absent. In addition, when analyzing a MWCNTs scaffold on the surface of sample S1 (Fig. 7B), the average ID/IG ratio is about 1.53. That is higher than the ratio calculated from MWCNTs collected in the electrolyte after 20 min PEO processing time (1.20). This means, to some extent, that the incorporation causes structural damages to the incorporated MWCNTs. Moreover, the relative intensity of the 2D (G') band is also diminished when compared to the as-received MWCNTs. Since that band results from the two-phonon second order scattering with creation of an inelastic phonon, it is indicative of long-range order [50]. Hence a lower intensity once again supports the hypothesis that disorder was introduced in the MWCNTs during their incorporation. The D" and G bands are also of great interest. Their respective intensities are comparable to those of the MWCNTs recovered from the electrolyte indicating that the formation of disorganized carbon structures is the same for incorporated particles and those still in the electrolyte.

3.3 In-depth characterization

TEM was used to detect and characterize the incorporated MWCNTs. As previously explained, TEM characterizations were carried out on alumina fragments collected after cleaving the surface of the processed samples. TEM observations were randomly carried out on several fragments in order to have an overview of the incorporation of MWCNTs throughout the overall coating thickness, from the interface aluminum/alumina to the top-surface of the alumina coating. Fig. 8 displays representative TEM pictures of the collected fragments as well as the associated elemental mapping for aluminum, oxygen and carbon elements. From elemental mapping, it appears that the carbon element (Fig. 8 B) covers homogeneously fragments enriched in aluminum and oxygen (Figs. 8C and 8D). It suggests that MWCNTs scaffolds are embedded with or in grains of aluminum oxide. High resolution TEM pictures (Figs. 8E and 8F) show isolated extremities of a few MWCNTs with their walls clearly visible. The observed entangled MWCNTs appear to be highly curved with abnormally low curvature radii. It suggests a potential alteration of their structural integrity resulting from their incorporation. This observation is in good agreement with the previous micro-Raman analysis that evidence an increase in the ID/IG ratio for MWCNTs incorporated on the top-surface of the coating.

Even though the TEM observations confirm that MWCNTs are effectively incorporated through the structure of the PEO coating, no information regarding their specific location can be obtained. So, a close examination of the cross-section of the samples was performed in order to ascertain the penetration and repartition of MWCNTs inside the PEO oxide layer. Cross-section SEM micrographs of the processed samples are given in Fig. 9. The average thickness of the formed PEO coatings are tabulated in Table V. It appears that the overall thickness of the PEO oxide layer increases as the concentration of the dispersed MWCNTs increases. For sample S0, the average thickness approximates 35 µm while it is above 60 µm for samples S1, S2 and S3 processed in the presence of dispersed MWCNTs. However, although the introduction of MWCNTs into the electrolyte seems to enhance the growth kinetics of the PEO coating, their presence results in a more porous morphology. Considering sample S0, Fig. 9 shows that the produced oxide layer consists in a quite dense coating with fine pores at the top-surface. In contrast, the morphology of the PEO coatings formed in the presence of MWCNTs is clearly more porous and can be divided into two distinct sublayers: a porous outer one with large connecting pores and a dense inner sublayer located close to the substrate. In addition, the morphology of the S1, S2 and S3 coatings alternate between sections with very distinctive outer porous and inner dense sublayers and regions with only a porous layer composed of large and deep pores with a lack or loss of an inner dense sublayer. This juxtaposition can be seen in Fig. 9 for samples S2 and S3. Those regions depicting wide open pores throughout the whole thickness of the coating have been attributed to the more jagged regions observed during the top-surface examinations (Fig. 5 for S2, evidenced in red). Moreover, as the concentration of the dispersed MWCNTs increases, the thickness of the outer sublayer relative to the total thickness increases. As reported in Table V, for samples S1, S2 and S3, the part of the porous outer sublayer represents ~36 %, ~51 % and ~62 % of the total coating thickness, respectively. Moreover, the volume proportion of regions with and without inner dense sublayer was estimated by calculating their linear ratio over the observed cross-section of the samples (assuming that the ratio along a line is representative of the volume proportion). For samples S1, S2 and S3, the volume proportion of regions with inner dense sublayer are respectively 49 %, 33 % and 32 %.

Fig. 10 shows cross-section SEM micrographs of sample S3 treated with 3 g.L^{-1} of dispersed MWCNTs. It evidences the presence of nanotubes deep within the porous outer sublayer. As for top-surface observations, the nanotubes appear in the form of scaffolds that line the internal walls of pores. It is worth noting however, that no MWCNTs was observed through the dense inner sublayer of the PEO coatings. Comparing S1, S2 and S3, as was done for the top-surface SEM characterization, the nanotubes are observed more uniformly as the concentration of MWCNTs increases. For sample S1, many pores do not contain any nanotubes while for the sample S3, nanotubes can readily be found on the walls of almost any pore.

Micro-Raman spectroscopy measurements were performed along the cross-section of the investigated samples at the same location previously observed by SEM (Fig. 10). Fig. 11 shows the Raman spectra recorded at different depths over the thickness of sample S3 from the top- surface of the PEO coating down to the aluminum substrate. It confirms the presence of MWCNTs in depth through the porous layer. Indeed, the D and G bands are clearly observed throughout the whole porous layer of the coating. In contrast, no scattering band is detected on the Raman spectrum recorded in the dense inner sublayer at the interface with the aluminum, suggesting the absence of any significant quantity of MWCNTs in this specific region of the coating. This is in good agreement with previous SEM observations.

The distribution of carbon throughout the oxide layer was also evaluated using glow discharge emission spectroscopy (GDOES). As previously explained in the experimental section, and in order to take into account the heterogeneous morphology of the PEO coatings inducing variations in the erosion speed, the GDOES elements profiles in Fig. 12 are qualitatively displayed as a function of the sputtering time. Fig. 12A shows the elemental profiles in aluminum, oxygen and carbon through the oxide layer for sample S1. More specifically, the profiles in carbon for samples S0 and S1 are compared in Fig. 12B. It is also worth mentioning that for sample S0, the GDOES analysis was stopped after 900 s compared to 2000 s for sample S1. It is explained by considering the fact that the oxide layer for sample S0 is much thinner (~30 µm) than that for sample S1 (~80 µm), the aluminum substrate being therefore reached after a shorter erosion time. As displayed in Fig. 12A, the variations of the oxygen and aluminum element profile can be used to indicate the transition from the oxide layer to the substrate. Indeed, after about 1000 s erosion time, the signal of oxygen gradually decreases while the signal of aluminum inversely increases, indicating the transition from the oxide coating to the aluminum substrate. Regarding Fig. 12B, within the first few seconds, the raw signal for the carbon element starts high and sharply decreases for both the samples S0 and S1. One can legitimately attribute this behavior to the presence of organic contaminants on the extreme surface. Beyond the very first few seconds, the carbon profile significantly differs between the two samples. Sample S0 presents a profile in carbon that rapidly falls down below the detection limit (10^{-3} V) in less than 200 s with no further variations. By contrast, for sample S1, carbon remains still detected until approximately 1500 s sputtering time, suggesting that carbon has been introduced deep within the coating.

3.4 Discussion about incorporation mechanisms

Regarding all the obtained results, a few propositions regarding the incorporation mechanisms can be suggested. Indeed, it is thought that the main driving force for particle accumulation within the coating is from particles being migrated into discharge pores left after the extinction of a micro discharge on the surface of the growing oxide. The collapse of the discharge channel leaves a local void that is filled with electrolyte and provided that the dispersed particles are smaller than the opening left after the micro discharge, they are dragged in with the electrolyte and deposited on the walls of the porosity network. This theory implies that: (i) bigger micro discharges generate larger channels, meaning that a greater volume of electrolyte may rush in and drag along a greater amount of particles, and (ii) the mechanism by which particles accumulate in the coating is rather violent and unequal throughout the process duration given that the repartition, lifetime and size of the surface micro discharges changes with time as evidenced in previous studies [51]. In this study, the opaqueness of the electrolyte with dispersed MWCNTs prevents the optical characterization from either fast imaging or optical emission spectroscopy. However, the observed morphology with wide open porosities throughout the whole coating thickness for samples processed with MWCNTs dispersed in the electrolyte are thought to result from high energy discharges traversing the whole oxide layer and melting-redepositing a substantial proportion of the growing coating resulting in a highly irregular network of large open porosities. Those regions were shown to preferentially accumulate MWCNTs. This observation is in accordance with the aforementioned mechanism such that the regions almost exclusively composed of an outer porous sublayer would result from the combination of high energy micro discharging events followed by infiltration of MWCNTs containing electrolyte. Also, the presence of particles in the electrolyte impacts the micro discharges. Indeed, the reference sample S0 did not display the same morphology as S1, S2 and S3 despite being processed in identical conditions if not for the absence of MWCNTs in the electrolyte. In addition, the observations regarding the degradation of the incorporated MWCNTs can be linked to this mechanism. Indeed, the incorporation mechanism requires the dispersed particles to be in close vicinity of a micro discharge and thus to be subjected to a succession of "severe" events (high local temperature, radical species, shockwaves from cavitation, mechanical compressive stress). This explains why the sharp increase in defects in the MWCNTs was observed for the incorporated particles and not those remaining in the electrolyte after the PEO treatment. Concomitantly, the aforementioned incorporation mechanism explains why the presence of MWCNTs was mostly observed in the outer porous layer that is more readily infiltrated by the electrolyte compared with the inner dense layer.

Although most of the MWCNTs found throughout the layer were present as scaffolds of different sizes, some individual MWCNTs are also scattered in the pores of the coating. Finally, some bridging MWCNTs were observed connecting across separate sections of the oxide as displayed in Fig. 13. It is however not readily possible to definitely confirm the nature of the bridging structures. Indeed, given that their dimensions are of the nanoscale in thickness, any available characterization technique would have either too low spatial resolution (Raman) or too low sampling size to get a chance to collect such a structure without destroying it (TEM). However, given that the dimensions and shape match those of the MWCNTs, and that this observation was not made for samples treated without MWCNTs, it is still highly likely that those bridges are indeed MWCNTs properly embedded in the matrix joining two separate sections. The importance of this information resides in the fact that the bridging MWCNTs may very well indicate that some of the incorporated particles are not visible for they are embedded in the oxide. This probably results from particles being trapped inside molten alumina resulting from a discharge event. As the molten alumina is quenched after the extinction of the micro-discharges, it can crack from thermomechanical stresses and reveal the entrapped MWCNTs thus appearing as bridging structures.

4. Conclusions

The present study detailed the incorporation of multi-walled carbon nanotubes (MWCNTs) into the plasma electrolytic oxidation alumina coating formed on an aluminum alloy when the process is carried out in a silicate-based electrolyte wherein various amounts of MWCNTs were dispersed. In particular, the main objective was to take advantage of a combination of characterization techniques to definitely assess the presence of MWCNTs both on the top-surface but also throughout the thickness of the PEO alumina coating. The following main conclusions can be drawn:

- Cross-checked results from various analysis ensure proper characterization of the in-depth incorporation of MWCNTs. Most notably, it was evidenced that MWCNTs preferentially incorporate throughout the porous outer sublayer of the coating rather than in the denser inner sublayer.
- MWCNTs were also shown to have a significant impact on the final morphology of the PEO coating. Indeed, higher amounts of MWCNTs dispersed in the electrolyte results in a thicker yet more porous alumina layer. To add to that, the coating is composed of regions of high irregularity and porosity throughout the whole thickness of the coating and regions with an outer porous layer and an inner denser layer.
- For the first time, it was also established that the MWCNTs experienced some degree of degradation during their incorporation into PEO alumina coating. Indeed, both STEM/EDX imaging and micro-Raman spectroscopy measurements revealed

a decrease in the structural integrity of the MWCNTs that could reasonably be assigned to the severe mechanical and thermodynamic conditions imposed by the PEO discharge regime.

Finally, based on the collected results, some precisions regarding the incorporation mechanisms were proposed. The heterogeneous distribution of MWCNTs throughout the PEO coating along with their presence were exclusively detected in the pores of the coating. This suggests that the main driving force for MWCNT incorporation during PEO treatments is electrolyte infiltration/deposition.

Acknowledgments

- This work was supported by the French Government through the programme “Investissements d’avenir" operated by the French National Research Agency (ANR) and referenced to as ANR-11-LABX-0008-01 (‘LabEx DAMAS’).
- This work was also partly supported by the Conseil Régional de la Région Grand Est for granting C. Da Silva Tousch PhD work under decision 19_GE8_049.
- The authors would like to acknowledge contributions of the following:
    - The competence cluster on electron microscopy (CC 3M) at Institut Jean Lamour for providing advice in SEM observations as well as performing all TEM and EDX analyses.
    - Dr. C. Herold, Dr. S. Cahen and Dr. S. Fontana for providing valuable advice in CNTs analyses.
    - The competence cluster on optics and lasers (CC COL) at Institut Jean Lamour for providing advice in micro-Raman spectroscopy.

Data availability

The data that support the findings of this study are available from the corresponding author, J. Martin, upon reasonable request.

Contribution of each author:

C. Da Silva Tousch: conceptualization, methodology, formal analysis, investigation, writing original draft, visualization.

J. Martin: conceptualization, writing - review & editing, visualization, supervision, funding acquisition, project administration.

G. Marcos: investigation, writing - review & editing.

T. Czerwiec: supervision, writing - review & editing, funding acquisition, project administration.

G. Henrion: supervision, writing - review & editing, funding acquisition, project administration.

Additional information

The authors declare no competing financial interests.

List of references

[1] A. L. Yerokhin, X. Nie, A. Leyland, A. Matthews, S.J. Dowey, Plasma electrolysis for surface engineering, Surf. Coat. Technol. 122 (1999) 73–93. doi: 10.1016/S0257-8972(99)00441-7.

[2] J. A. Curran, T. W. Clyne, Porosity in plasma electrolytic oxide coatings, Acta Mater. 54 (2006) 1985–1993. doi: 10.1016/j.actamat.2005.12.029.

[3] A. Fattah-alhosseini, M. Molaei, K. Babaei, The effects of nano- and micro-particles on properties of plasma electrolytic oxidation (PEO) coatings applied on titanium substrates: A review, Surf. Interfaces 21 (2020) 100659. doi: 10.1016/j.surfin.2020.100659.

[4] J. Martin, A. Nominé, V. Ntomprougkidis, S. Migot, S. Bruyère, F. Soldera, T. Belmonte, G. Henrion, Formation of a metastable nanostructured mullite during Plasma Electrolytic Oxidation of aluminium in ‘soft’ regime condition, Mater. Des. 180 (2019) 107977. doi: 10.1016/j.matdes.2019.107977.

[5] V. Dehnavi, B. L. Luan, D. W. Shoesmith, X. Y. Liu, S. Rohani, Effect of duty cycle and applied current frequency on plasma electrolytic oxidation (PEO) coating growth behavior, Surf. Coat. Technol. 226 (2013) 100–107. doi: 10.1016/j.surfcoat.2013.03.041.

[6] X. Lu, M. Mohedano, C. Blawert, E. Matykina, R. Arrabal, K.U. Kainer, M.L. Zheludkevich, Plasma electrolytic oxidation coatings with particle additions – A review, Surf. Coat. Technol. 307 (2016) 1165-1182. doi: 10.1016/j.surfcoat.2016.08.055.

[7] A. Fattah-alhosseini, R. Chaharmahali, K. Babaei, Effect of particles addition to solution of plasma electrolytic oxidation (PEO) on the properties of PEO coatings formed on magnesium and its alloys: A review, J. Magnes. Alloy 8 (2020) 799–818. doi: 10.1016/j.jma.2020.05.001.

[8] X. Lu, C. Blawert, Y. Huang, H. Ovri, M. L. Zheludkevich, K. U. Kainer, Plasma electrolytic oxidation coatings on Mg alloy with addition of SiO2 particles, Electrochim. Acta 187 (2016) 20–33. doi: 10.1016/j.electacta.2015.11.033.

[9] X. Lu, C. Blawert, M. L. Zheludkevich, K. U. Kainer, Insights into plasma electrolytic oxidation treatment with particle addition, Corrosion Sci. 101 (2015) 201–207. doi: 10.1016/j.corsci.2015.09.016.

[10] K. M. Lee, B. U. Lee, S. Il Yoon, E. S. Lee, B. Yoo, D. H. Shin, Evaluation of plasma temperature during plasma oxidation processing of AZ91 Mg alloy through analysis of the melting behavior of incorporated particles, Electrochim. Acta 67 (2012) 6–11. doi: 10.1016/j.electacta.2012.01.053.

[11] C. Blawert, S. P. Sah, J. Liang, Y. Huang, D. Höche, Role of sintering and clay particle additions on coating formation during PEO processing of AM50 magnesium alloy, Surf. Coat. Technol. 213 (2012) 48–58. doi: 10.1016/j.surfcoat.2012.10.013.

[12] G. Rapheal, S. Kumar, N. Scharnagl, C. Blawert, Effect of current density on the microstructure and corrosion properties of plasma electrolytic oxidation (PEO) coatings on AM50 Mg alloy produced in an electrolyte containing clay additives, Surf. Coat. Technol. 289 (2016) 150–164. doi: 10.1016/j.surfcoat.2016.01.033.

[13] J. Liang, L. Hu, J. Hao, Preparation and characterization of oxide films containing crystalline TiO2 on magnesium alloy by plasma electrolytic oxidation, Electrochim. Acta 52 (2007) 4836–4840. doi: 10.1016/j.electacta.2007.01.059.

[14] K. M. Lee, K. R. Shin, S. Namgung, B. Yoo, D. H. Shin, Electrochemical response of ZrO2-incorporated oxide layer on AZ91 Mg alloy processed by plasma electrolytic oxidation, Surf. Coat. Technol. 205 (2011) 3779–3784. doi: 10.1016/j.surfcoat.2011.01.033.

[15] M. Daroonparvar, M. A. M. Yajid, N. M. Yusof, H. R. Bakhsheshi-Rad, Preparation and corrosion resistance of a nanocomposite plasma electrolytic oxidation coating on Mg-1%Ca alloy formed in aluminate electrolyte containing titania nano-additives, J. Alloy. Compd. 688 (2016) 841–857. doi: 10.1016/j.jallcom.2016.07.081.

[16] Spragg, S. P.. Electrophoresis, In R.A. Meyers (Ed.) *Encyclopedia of Physical Science and Technology.*, Academic Press 2004 (pp. 363–378).

[17] M. O'Hara, S. C. Troughton, R. Francis, T. W. Clyne, The incorporation of particles suspended in the electrolyte into plasma electrolytic oxidation coatings on Ti and Al substrates, Surf. Coat. Technol. 385 (2020) 125354. doi: 10.1016/j.surfcoat.2020.125354.

[18] Y. Chen, X. Lu, C. Blawert, M.L. Zheludkevich, T. Zhang, F. Wang, Formation of self-lubricating PEO coating via in-situ incorporation of PTFE particles, Surf. Coat. Technol. 337 (2018) 379-388. doi: 10.1016/j.surfcoat.2018.01.022

[19] V. N. Popov, Carbon nanotubes: Properties and application, Mater. Sci. Eng. R-Rep., 43 (2004) 61–102. doi: 10.1016/j.mser.2003.10.001.

[20] R. S. Costa, A. Guedes, A. M. Pereira, C. Pereira, Fabrication of all-solid-state textile supercapacitors based on industrial-grade multi-walled carbon nanotubes for enhanced energy storage, J. Mater. Sci. 55 (2020) 10121–10141. doi: 10.1007/s10853-020-04709-0.

[21] R. Metz, L. Diaz, R. Aznar, L. Alvarez, V. Flaud, S. Ananthakumar, J.L. Bantigniesa, Carbon nanotube-epoxy composites: The role of acid treatment in thermal and electrical conductivity, Exp. Heat Transf. 30 (2017) 66–76. doi: 10.1080/08916152.2016.1161675.

[22] Roham Rafiee 2017. *Carbon Nanotube-Reinforced Polymers*. Elsevier.

[23] A. Nieto, A. Agarwal, D. Lahiri, A. Bisht, S. R. Bakshi, 2021. *Carbon Nanotubes* (1st ed) . CRC Press.

[24] E. Flahaut, S. Rul, F. Lefèvre-Schlick, C. Laurent, A. Peigney, Carbon nanotubes-ceramic composites, Ceram. Trans. 148 (2004) 71–82. doi: 10.1533/9781845691066.3.309.

[25] C. A. Isaza M, B. Zuluaga D, J. S. Rudas, H. A. Estupiñán D, J. M. Herrera R, J. M. Meza, Mechanical and Corrosion Behavior of Plasma Electrolytic Oxidation Coatings on AZ31B Mg Alloy Reinforced with Multiwalled Carbon Nanotubes, J. Mater. Eng. Perform. 29 (2020) 1135–1145. doi: 10.1007/s11665-020-04633-z.

[26] M. Hwang, W. Chung, Effects of a carbon nanotube additive on the corrosion-resistance and heat-dissipation properties of plasma electrolytic oxidation on AZ31 magnesium alloy, Materials 11 (2018) 2438. doi: 10.3390/ma11122438.

[27] R. Kara, H. Zengin, Tribological and Electrochemical Corrosion Properties of CNT-Incorporated Plasma Electrolytic Oxidation (PEO) Coatings on AZ80 Magnesium Alloy, Acta Metall. Sin. - Engl. (2022), doi: 10.1007/s40195-021-01363-6.

[28] F. Aydin, A. Ayday, M. E. Turan, H. Zengin, Role of graphene additive on wear and electrochemical corrosion behaviour of plasma electrolytic oxidation (PEO) coatings on Mg–MWCNT nanocomposite, Surf. Eng. 36 (2020) 791–799. doi: 10.1080/02670844.2019.1689640.

[29] Y. Guo, L. Xu, J. Luan, Y. Wan, R. Li, Effect of carbon nanotubes additive on tribocorrosion performance of micro-arc oxidized coatings on Ti6Al4V alloy, Surf. Interfaces 28 (2022) 101626. doi: 10.1016/j.surfin.2021.101626.

[30] M. Daavari, M. Atapour, M. Mohedano, R. Arrabal, E. Matykina, A. Taherizadeh, Biotribology and biocorrosion of MWCNTs-reinforced PEO coating on AZ31B Mg alloy, Surf. Interfaces 22 (2021) 100850. doi: 10.1016/j.surfin.2020.100850.

[31] Y. Yürektürk, F. Muhaffel, M. Baydoğan, Characterization of micro arc oxidized 6082 aluminum alloy in an electrolyte containing carbon nanotubes, Surf. Coat. Technol. 269 (2015) 83–90. doi: 10.1016/j.surfcoat.2014.12.058.

[32] K. M. Lee, Y. G. Ko, D. H. Shin, Incorporation of multi-walled carbon nanotubes into the oxide layer on a 7075 Al alloy coated by plasma electrolytic oxidation: Coating structure and corrosion properties, Curr. Appl. Phys. 11 (2011) S55–S59. doi: 10.1016/j.cap.2011.07.009.

[33] M. Sabouri, S. M. Mousavi Khoei, Plasma electrolytic oxidation in the presence of multiwall carbon nanotubes on aluminum substrate: Morphological and corrosion studies, Surf. Coat. Technol. 334 (2018) 543–555. doi: 10.1016/j.surfcoat.2017.10.045.

[34] K. M. Lee, Y. G. Ko, D. H. Shin, Incorporation of carbon nanotubes into micro-coatings film formed on aluminum alloy via plasma electrolytic oxidation, Mater. Lett. 65 (2011) 2269–2273. doi: 10.1016/j.matlet.2011.04.001.

[35] K. Hyun, J. H. Lee, S. J. Kim, Incorporation of multi-walled carbon nanotubes into oxide layer formed on al alloy by plasma electrolytic oxidation, Surf. Rev. Lett. 27 (2020) 1–7. doi: 10.1142/S0218625X20500079.

[36] K. E. Geckeler, T. Premkumar, Carbon nanotubes: Are they dispersed or dissolved in liquids?, Nanoscale Res. Lett. 6 (2011) 2–4. doi: 10.1186/1556-276X-6-136.

[37] I. M. Mahbubul, C. Tet, S. S. Khaleduzzaman, I. M. Shahrul, R. Saidur, B. D. Long, M. A. Amalina, Effect of Ultrasonication Duration on Colloidal Structure and Viscosity of Alumina–Water Nanofluid. Ind. Eng. Chem. Res. 53 (2014) 6677-6684. doi: 10.1021/ie500705j.

[38] F. Jaspard-Mécuson, T. Czerwiec, G. Henrion, T. Belmonte, L. Dujardin, A. Viola, J. Beauvir, Tailored aluminium oxide layers by bipolar current adjustment in the Plasma Electrolytic Oxidation (PEO) process, Surf. Coat. Technol. 201 (2007) 8677–8682. doi: 10.1016/j.surfcoat.2006.09.005.

[39] B.J. Griffin, A Comparison of Conventional Everhart-Thornley Style and In-Lens Secondary Electron Detectors—A Further Variable in Scanning Electron Microscopy, Scanning 33 (2011) 162-173. doi: 10.1002/sca.20255.

[40] E. F. Antunes, A. O. Lobo, E. J. Corat, V. J. Trava-Airoldi, A. A. Martin, C. Veríssimo, Comparative study of first- and second-order Raman spectra of MWCNT at visible and infrared laser excitation, Carbon 44 (2006) 2202–2211. doi: 10.1016/j.carbon.2006.03.003.

[41] W. Li, H. Zhang, C. wang, Y. Zhang, L. Xu, K. Zhu, S. Xie, Raman characterization of aligned carbon nanotubes produced by thermal decomposition of hydrocarbon vapor, Appl. Phys. Lett. 70 (1997) 2684–2686. doi: 10.1063/1.118993.

[42] M. V. Ivanova, C. Lamprecht, M. Jimena Loureiro, J. Torin Huzil, M. Foldvari, Pharmaceutical characterization of solid and dispersed carbon nanotubes as nanoexcipients, Int. J. Nanomed. 7 (2012) 403–415. doi: 10.2147/ijn.s27442.

[43] A. Merlen, J. G. Buijnsters, C. Pardanaud, A guide to and review of the use of multiwavelength Raman spectroscopy for characterizing defective aromatic carbon solids: From graphene to amorphous carbons, Coatings 7 (2017) 153. doi: 10.3390/coatings7100153.

[44] T. Jawhari, A. Roid, J. Casado, Raman spectroscopic characterization of some commercially available carbon black materials, Carbon 33 (1995) 1561–1565. doi: 10.1016/0008-6223(95)00117-V.µ.

[45] Y. Wang, D. Vasileva, S. P. Zustiak, I. Kuljanishvili, Raman spectroscopy enabled investigation of carbon nanotubes quality upon dispersion in aqueous environments, Biointerphases 12 (2017) 011004. doi: 10.1116/1.4978922.

[46] W. Bai, A. Raghavendra, R. Podila, J. M. Brown, Defect density in multiwalled carbon nanotubes influences ovalbumin adsorption and promotes macrophage activation and CD4+ T-cell proliferation, Int. J. Nanomed. 11 (2016) 4357–4371. doi: 10.2147/IJN.S111029.

[47] Y. C. Choi, K. I. Min, M. S. Jeong, Novel method of evaluating the purity of multiwall carbon nanotubes using raman spectroscopy, J. Nanomater. 2013 (2013) 1-6. doi: 10.1155/2013/615915.

[48] R. O. Hussein, D. O. Northwood, X. Nie, Coating growth behavior during the plasma electrolytic oxidation process, J. Vac. Sci. Technol. A Vac. Surf. Films 28 (2010) 766–773. doi: 10.1116/1.3429583.

[49] G. Sundararajan, L. Rama Krishna, Mechanisms underlying the formation of thick alumina coatings through the MAO coating technology, Surf. Coat. Technol. 167 (2003) 269–277. doi: 10.1016/S0257-8972(02)00918-0.

[50] R. A. DiLeo, B. J. Landi, R. P. Raffaelle, Purity assessment of multiwalled carbon nanotubes by Raman spectroscopy, J. Appl. Phys. 10 (2007) 064307. doi: 10.1063/1.2712152.

[51] J. Martin, A. Nominé, F. Brochard, J.-L. Briançon, C. Noël, T. Belmonte, T. Czerwiec, G. Henrion, Delay in micro-discharges appearance during PEO of Al: Evidence of a mechanism of charge accumulation at the electrolyte/oxide interface, Appl. Surf. Sci. 410 (2017) 29–41. doi: 10.1016/j.apsusc.2017.03.088.

List of tables

Table I: Elemental composition of the 1050 aluminum substrate.

Element	**Cu**	**Mg**	**Mn**	**Si**	**Fe,Ti,Zn**	**Al**
wt.%	0.05	<0.05	<0.05	<0.25	<0.5	Balance

Table II: Properties of the as-received multi-walled carbon nanotubes (MWCNTS). SEM, TEM and TGA stand for scanning electron microscopy, transmission electron microscopy, and thermogravimetric analysis, respectively.

Aggregate dimensions	**Purity**	**External diameter**	**Length**
200 - 1000 µm (SEM)	93 wt.% (TGA)	12 - 20 nm (TEM)	0.1 - 10 µm (TEM)

Table III: MWCNTs and sodium dodecyl sulfate (SDS) surfactant content in electrolyte for the different samples labeled S0, S1, S2 and S3.

Sample	**S0**	**S1**	**S2**	**S3**
[MWCNTs] (g.L^{-1})	0	1	2	3
[SDS] (g.L^{-1})	0	1	2	3

Table IV: Band position, name and interpretation of the Raman spectra of MWCNTs:

Band position	Band name	Interpretation	Ref
1150 cm-1	D” or D3	Presence of soot and amorphous carbon	43
1350 cm^{-1}	D	Defect dependent, associated with edges and disorder in the structure	40-42
1500 cm^{-1}	$G_{amorphous}$ or D4	Presence of disordered and amorphous carbons	44
1580 cm^{-1}	G	High frequency first order mode (E_{2g}) from graphene-like structures	43
1620 cm^{-1}	D’	Defect dependent	40
2450 cm^{-1}	D+D”	Second order scattering band	43
2700 cm^{-1}	2D or G’	Second order scattering band	40
2945 cm^{-1}	D+D’	Second order scattering band	40
3175 cm^{-1}	2G	Second order scattering band	40

Table V: Average roughness parameter Ra, average coating thickness measurement and corresponding standard deviation for all PEO samples. MWCNT+PEO sample measurements were differentiated in two categories given the large difference in thickness between regions with and without an inner dense sublayer. For samples S1, S2 and S3 the average thickness of the outer porous sublayer relative to the total oxide thickness is also given.

Sample	**S0**	**S1**	**S2**	**S3**
Roughness parameter Ra (μm)	3.2 ± 1.0	8.4 ± 1.1	8.0 ± 2.0	10.5 ± 2.1
Thickness in regions **with** a visible inner dense sublayer (μm)	35 ± 4	72 ± 11	76 ± 15	60 ± 11
Thickness in regions **without** inner dense sublayer (μm)	n.a.	100 ± 20	127 ± 21	100 ± 12
Average proportion of the outer sublayer (%)	n.a.	32	51	62

List of figure captions:

Figure 1: Schematic representation of the applied current waveform.

Figure 2: Bright-field TEM micrographs recorded (A) on the as-received MWCNTs powders and (B) on the dispersed MWCNTs after sonication treatment in electrolyte and complete drying.

Figure 3: Raman spectra (and the fitted Raman scattering bands of MWCNTs) recorded (A) on the as-received MWCNTs powder and (B) on the MWCNTs collected from the PEO electrolyte used for 20 min and after complete drying.

Figure 4: Top-surface photographs of the samples S0, S1, S2 and S3.

Figure 5 : Top-surface (SE mode) SEM micrographs recorded on samples S0 and S2. Sample S0 depicts a homogeneous surface appearance while S2 (also representative of S1 and S3) reveals an alternation of smoother regions and rugged regions (circled in red).

Figure 6: Top-surface (InLens mode) SEM micrographs recorded at different magnifications and locations over the surface of samples S1 (A, C and E) and S3 (B, D and F). MWCNTs are emphasized by red circles and arrows.

Figure 7: (A) Raman spectra recorded on the top-surface of samples S0, S1, S2 and S3. (B) Fitted scattering bands of the Raman spectrum recorded on the top-surface of sample S1.

Figure 8: High-resolution TEM micrographs showing entangled MWCNTs interlocked in alumina grains. (A) Bright-field STEM micrograph recorded on the PEO alumina coating (after micro-cleaving) of sample S3 and the associated STEM / EDX elemental maps in (B) carbon, (C) aluminum and (D) oxygen. (E, F) High-resolution TEM pictures. Image in (E) is an enlarged view of the region marked by a red square in A.

Figure 9: Cross-section (SE mode) SEM micrographs recorded at different magnifications on samples S0, S1, S2 and S3. Left column shows the regions where an outer porous sublayer and an inner dense sublayer (separated by a blue dotted line) are observed. Right column shows the regions where only a highly porous layer throughout the coating is observed for S1, S2 and S3.

Figure 10: Cross-section SEM micrographs of sample S3 recorded particularly in a very porous region at different magnifications over the cross-section (A, B) in SE mode and (C, D) in InLens mode.

Figure 11: Raman spectra recorded at different depths along a cross-section of sample S3 at the location indicated in Fig. 10(A).

Figure 12: (A) GDOES chemical profiles in elements C, Al and O recorded on sample S1 and (B) GDOES profiles of the carbon element recorded on samples S0 and S1. The transition from PEO coating to aluminum substrate for sample S1 is indicated on both graphs.

Figure 13: SEM micrographs (InLens mode) of polished cross-section recorded on sample S3 showing individual nanotubes interlocked in the PEO alumina structure (indicated by red arrows).

Figure 14: Schematic of the proposed incorporation mechanism. (A) Coating being processed with CNTs dispersed in the electrolyte. (B) Dielectric breakdown of the oxide layer. (C) Infiltration of the electrolyte in the pore network left after the extinction of the micro-discharge. (D) Cooling of the newly formed porous oxide. (E) CNT scaffolds lining the walls of the newly formed pores.

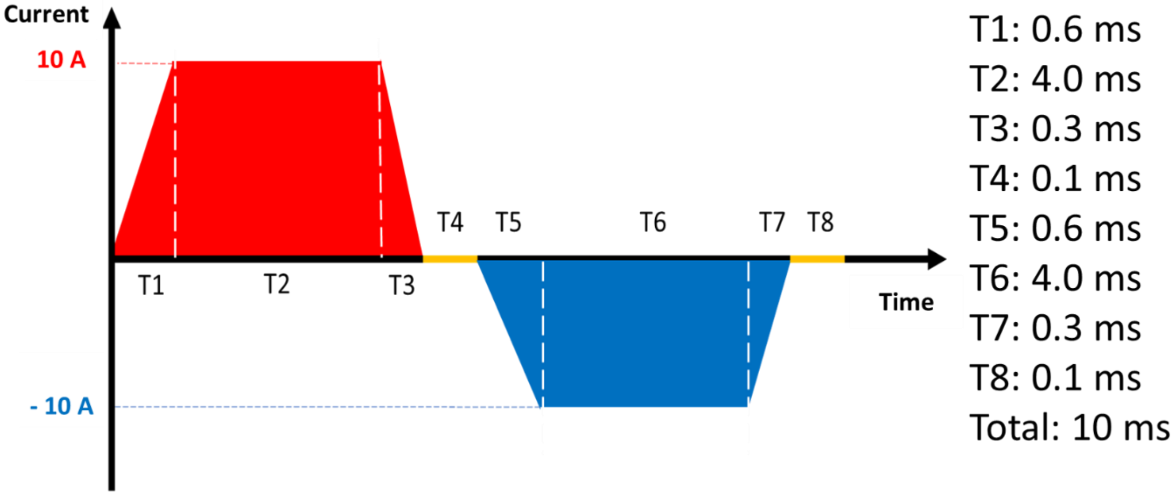
Current
10 A
- 10 A
T1
T2
T3
T4
T5
T6
T7
T8
Time
T1: 0.6 ms
T2: 4.0 ms
T3: 0.3 ms
T4: 0.1 ms
T5: 0.6 ms
T6: 4.0 ms
T7: 0.3 ms
T8: 0.1 ms
Total: 10 ms

Figure 1

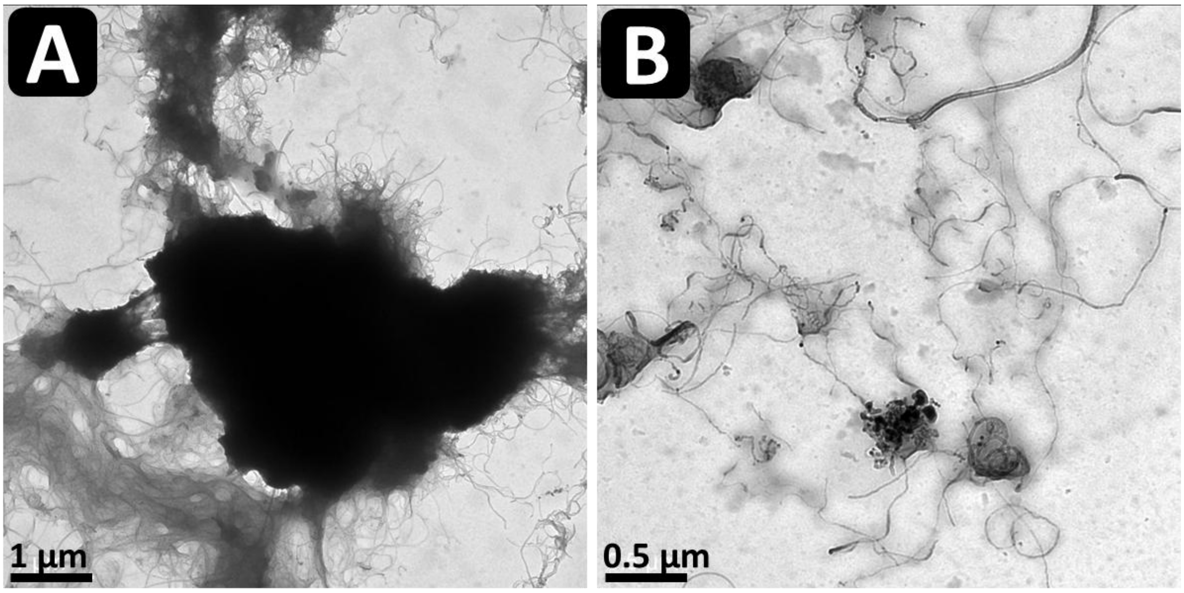

Figure 2

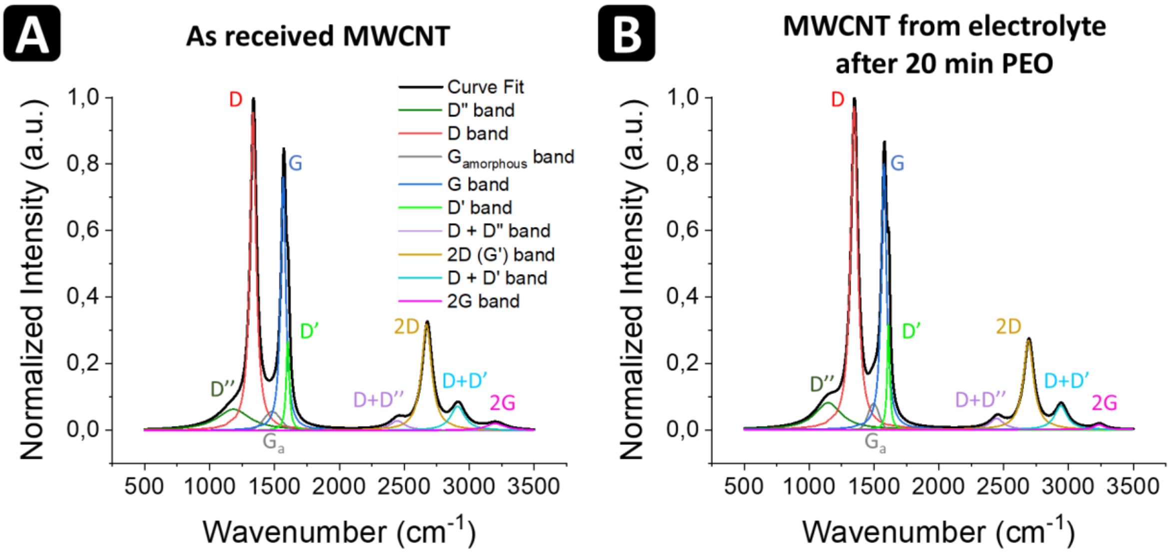
A
As received MWCNT
B
MWCNT from electrolyte after 20 min PEO
Normalized Intensity (a.u.)
1,0
0,8
0,6
0,4
0,2
0,0
Wavenumber (cm^{-1})
500
1000
1500
2000
2500
3000
3500
D
G
D'
2D
D+D'
2G
D''
D+D''
G$_a$
Curve Fit
D'' band
D band
G$_{amorphous}$ band
G band
D' band
D + D'' band
2D (G') band
D + D' band
2G band

Figure 3

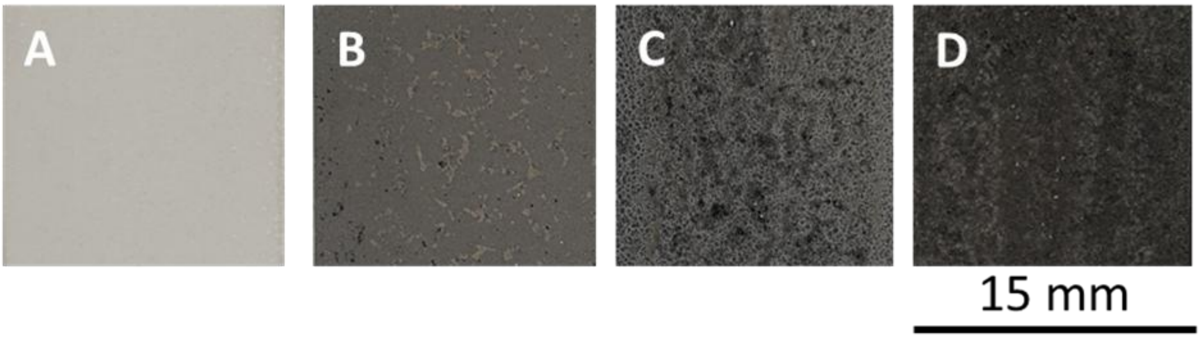

Figure 4

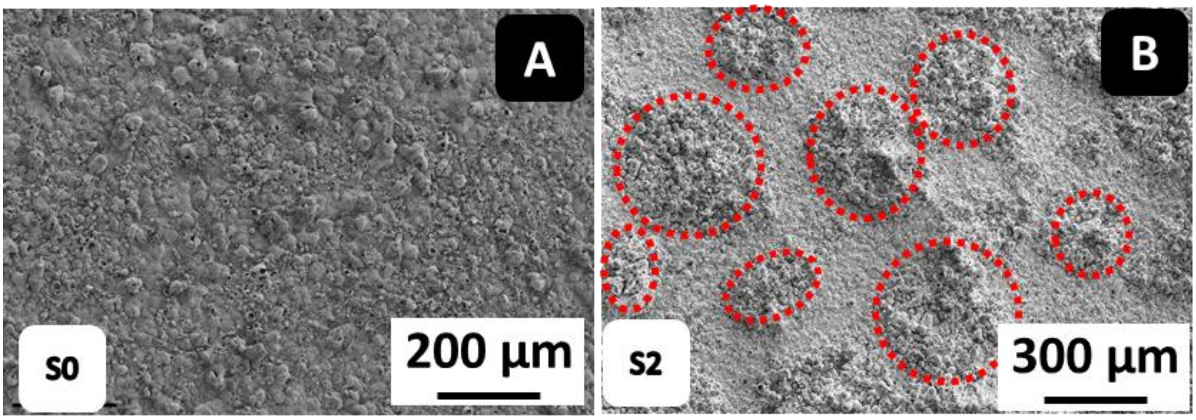

Figure 5

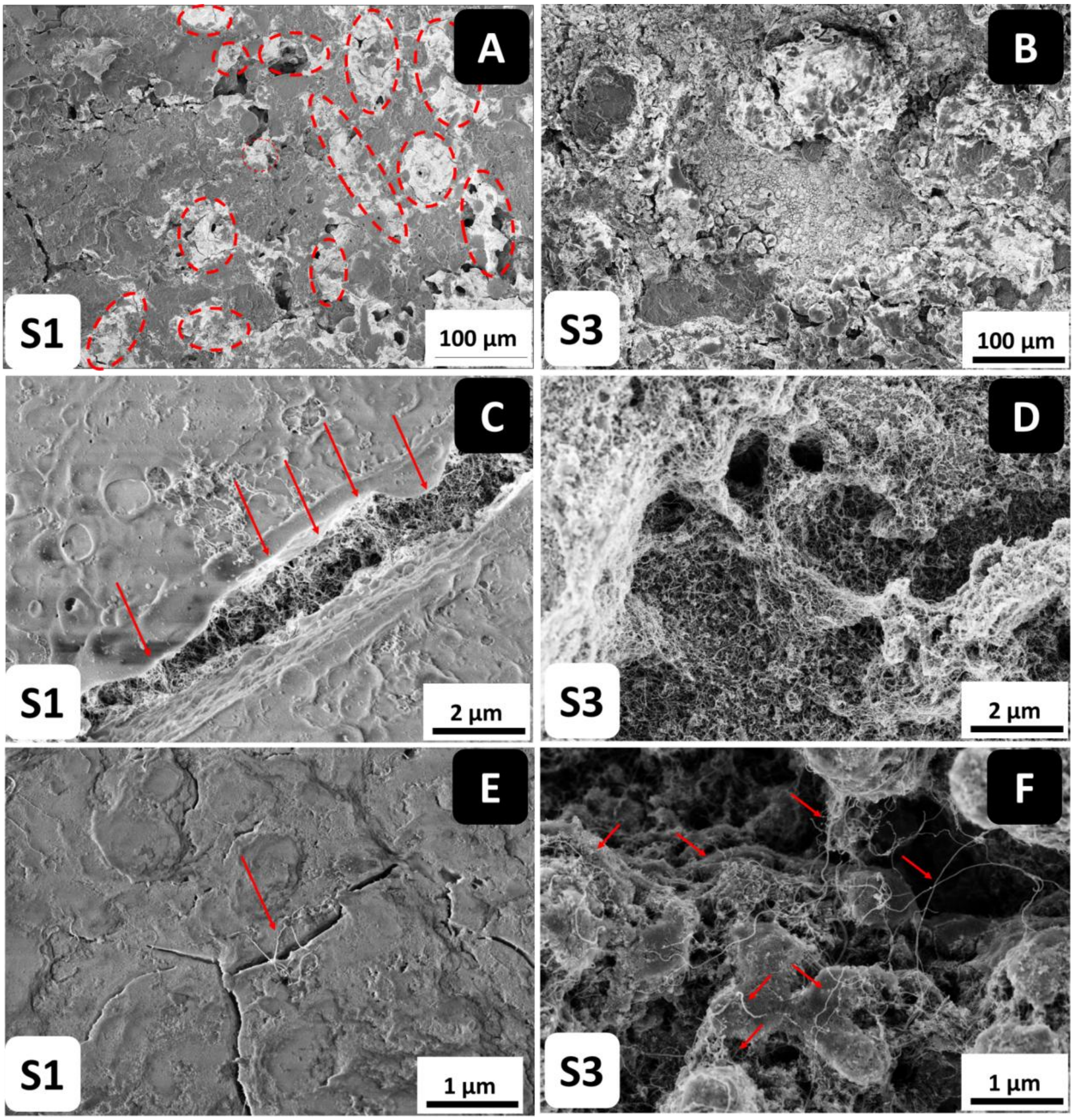

Figure 6

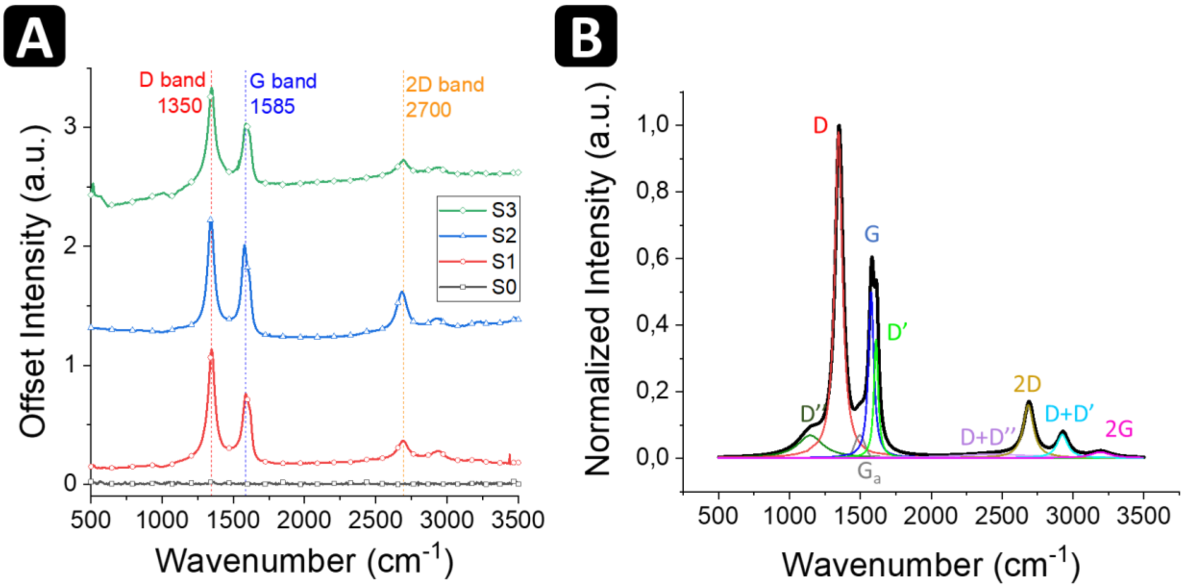
A
D band
1350
G band
1585
2D band
2700
S3
S2
S1
S0
Offset Intensity (a.u.)
0
1
2
3
500
1000
1500
2000
2500
3000
3500
Wavenumber (cm^{-1})
B
Normalized Intensity (a.u.)
1,0
0,8
0,6
0,4
0,2
0,0
D
G
D'
D''
G_a
2D
D+D''
D+D'
2G
500
1000
1500
2000
2500
3000
3500
Wavenumber (cm^{-1})

Figure 7

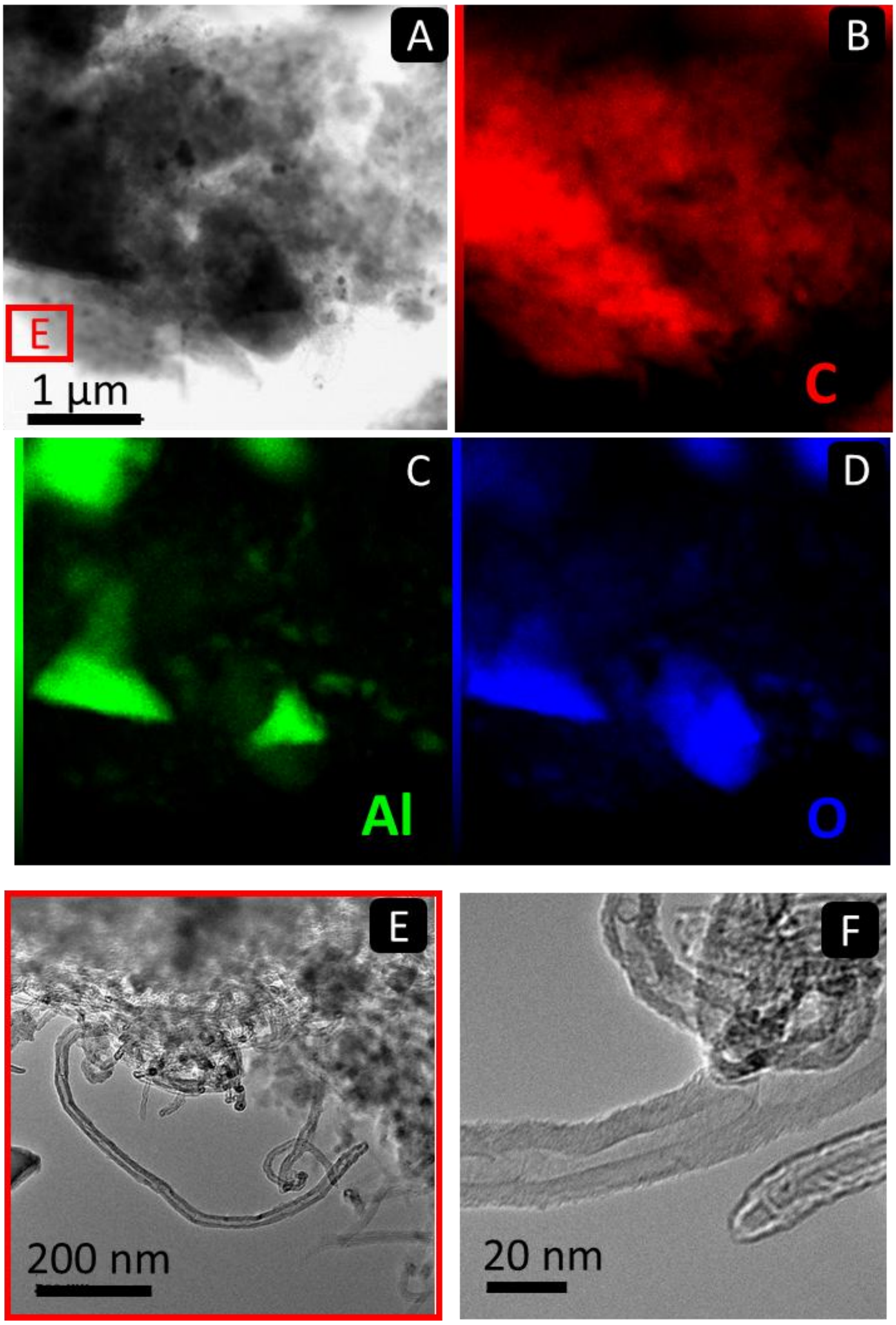

Figure 8

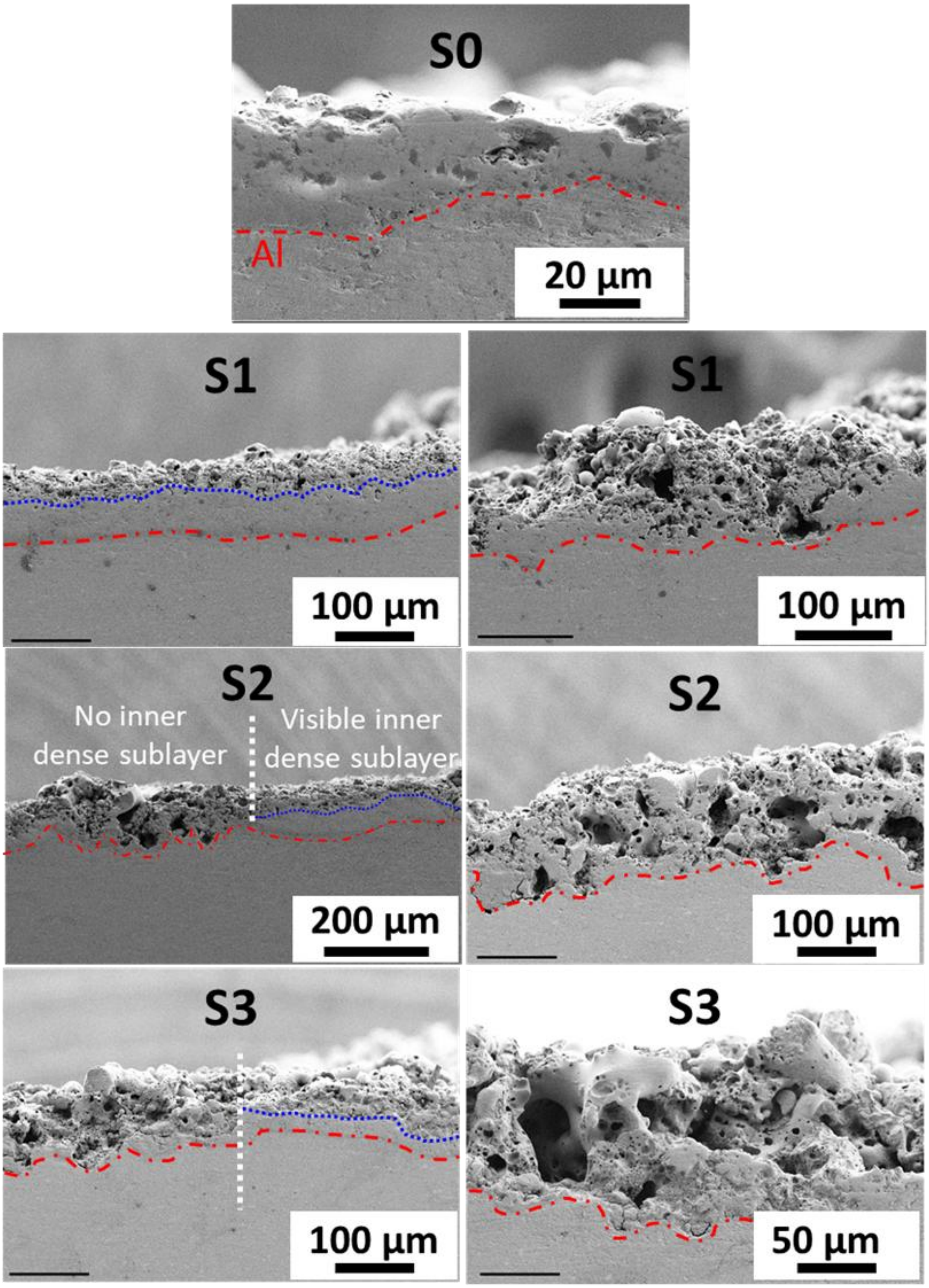
S0
Al
20 µm
S1
100 µm
S1
100 µm
S2
No inner dense sublayer
Visible inner dense sublayer
200 µm
S2
100 µm
S3
100 µm
S3
50 µm

Figure 9

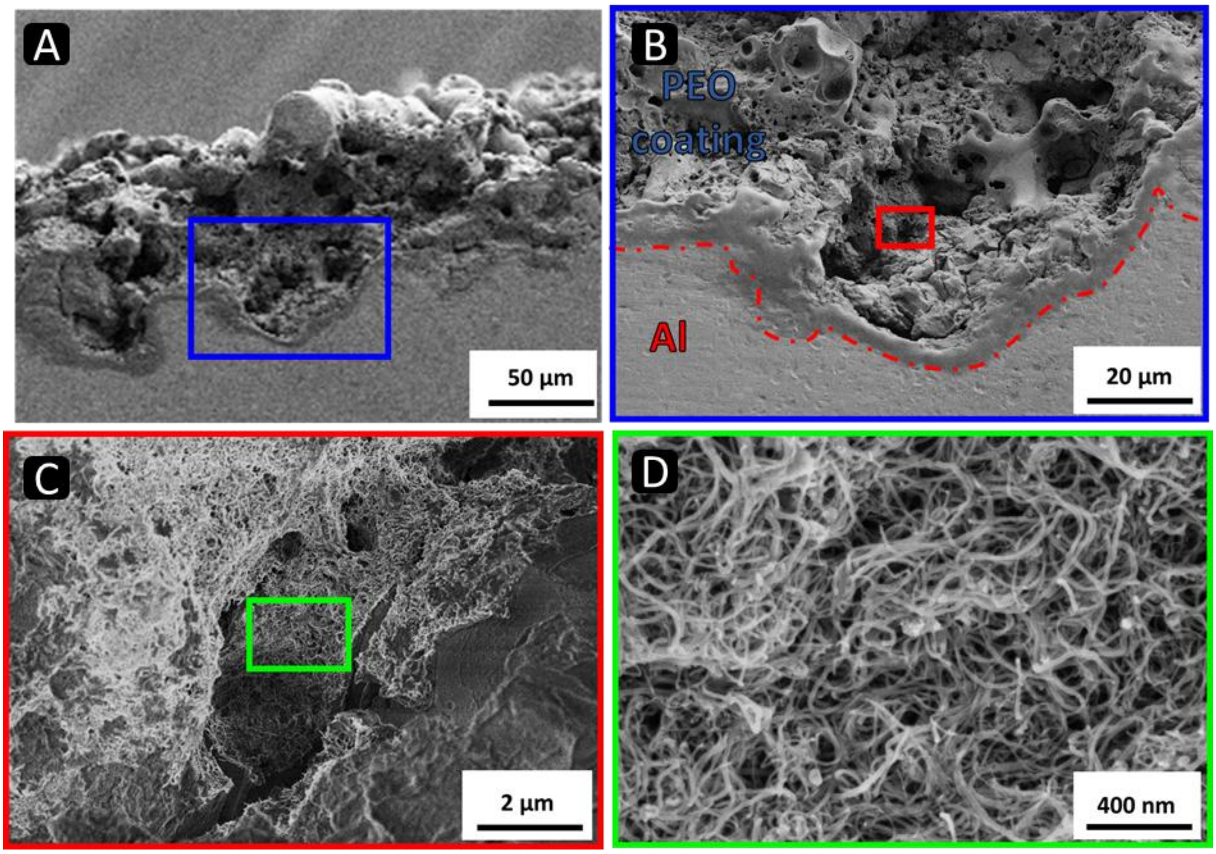

Figure 10

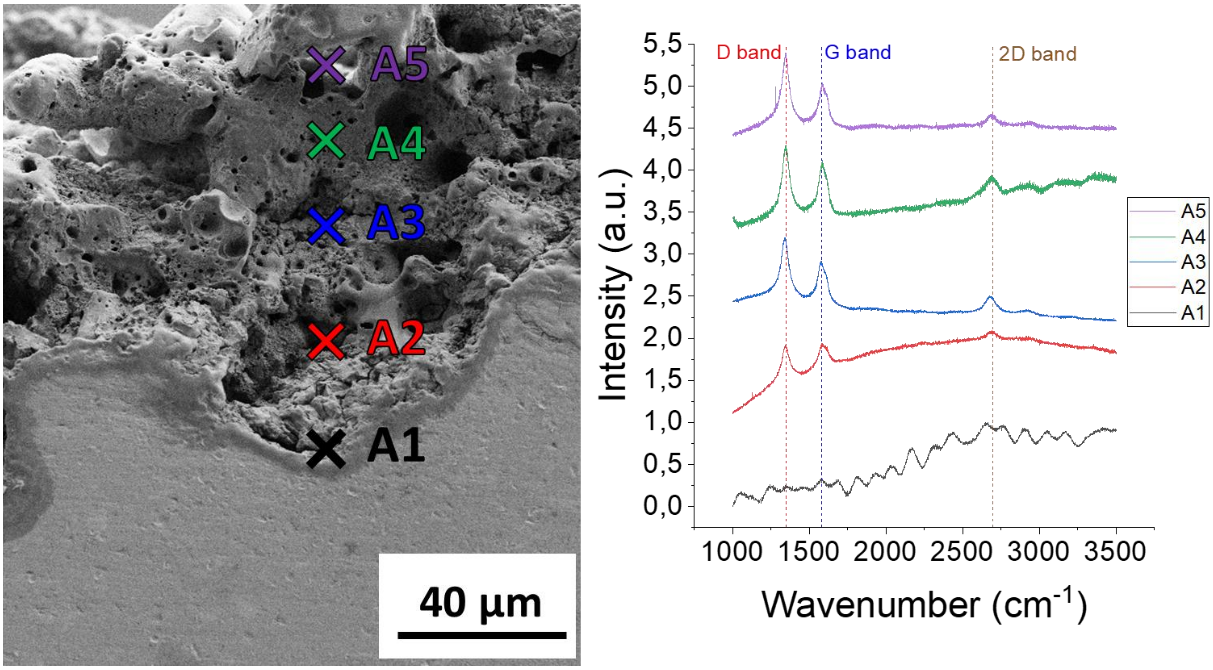
A5
A4
A3
A2
A1
40 µm
D band
G band
2D band
Intensity (a.u.)
5,5
5,0
4,5
4,0
3,5
3,0
2,5
2,0
1,5
1,0
0,5
0,0
1000
1500
2000
2500
3000
3500
Wavenumber (cm^{-1})
A5
A4
A3
A2
A1

Figure 11

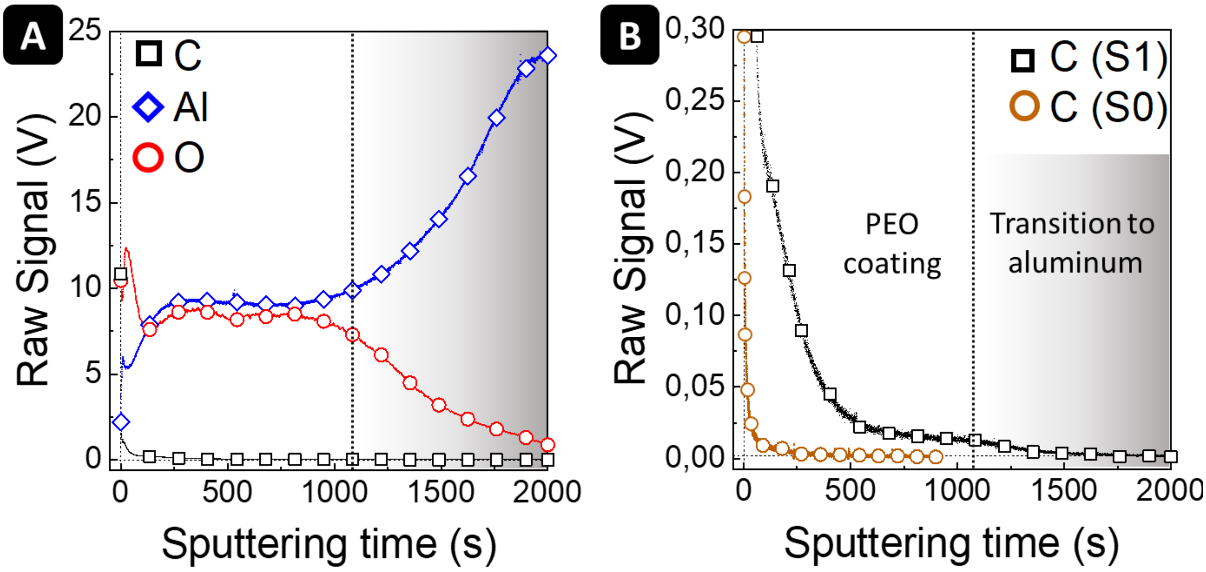
A
25
20
15
10
5
0
Raw Signal (V)
C
Al
O
0
500
1000
1500
2000
Sputtering time (s)
B
0,30
0,25
0,20
0,15
0,10
0,05
0,00
Raw Signal (V)
C (S1)
C (S0)
PEO coating
Transition to aluminum
0
500
1000
1500
2000
Sputtering time (s)

Figure 12

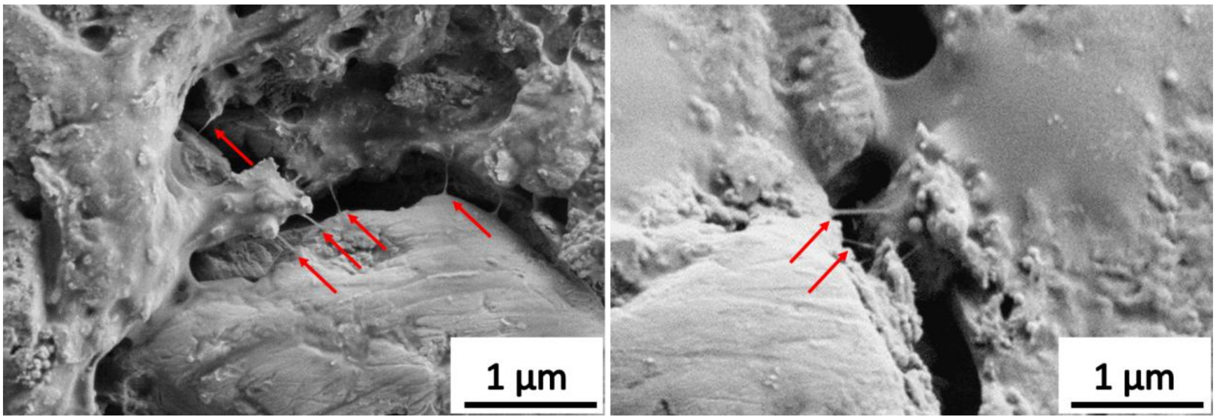

Figure 13

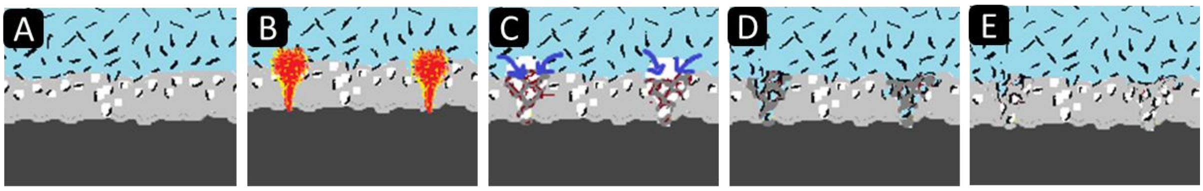

Discharge

Electrolyte Infiltration

CNT scaffolds in pores of newly formed alumina

Figure 14